Automatic Detection of Single Fluorophores in Live Cells

G. I. Mashanov and J. E. Molloy
Division of Physical Biochemistry, MRC National Institute for Medical Research, NW7 1AA, London, United Kingdom

ABSTRACT Recent developments in light microscopy enable individual fluorophores to be observed in aqueous conditions. Biological molecules, labeled with a single fluorophore, can be localized as isolated spots of light when viewed by optical microscopy. Total internal reflection fluorescence microscopy greatly reduces background fluorescence and allows single fluorophores to be observed inside living cells. This advance in live-cell imaging means that the spatial and temporal dynamics of individual molecules can be measured directly. Because of the stochastic nature of single molecule behavior a statistically meaningful number of individual molecules must be detected and their separate trajectories in space and time stored and analyzed. Here, we describe digital image processing methods that we have devised for automatic detection and tracking of hundreds of molecules, observed simultaneously, in vitro and within living cells. Using this technique we have measured the diffusive behavior of pleckstrin homology domains bound to phosphoinositide phospholipids at the plasma membrane of live cultured mammalian cells. We found that mobility of these membrane-bound protein domains is dominated by mobility of the lipid molecule to which they are attached and is highly temperature dependent. Movement of PH domains isolated from the tail region of myosin-10 is consistent with a simple random walk, whereas, diffusion of intact PLC-δ1 shows behavior inconsistent with a simple random walk. Movement is rapid over short timescales but much slower at longer timescales. This anomalous behavior can be explained by movement being restricted to membrane regions of 0.7 μm diameter.

INTRODUCTION

It is now 12 years since the first convincing report of single fluorophore imaging in aqueous solution (1). Since then, most of the technologies used—microscopes, lasers, and cameras—have changed rather little. However, the advent of the green fluorescent protein (2) (GFP) and increases in computing power (by ~100-fold) have revolutionized the way that we study fluorescent molecules in live biological cells. Digital image processing enables rapid, quantitative analysis of both static images and video sequences obtained by optical microscopy. Here, we report a single fluorophore detection algorithm (SFDA) that can be used to identify multiple individual fluorophores in a series of video images obtained by total internal reflection fluorescence microscopy (TIRFM). We also describe an automatic single particle tracking (ASPT) algorithm that is used to detect and track single fluorophores moving on the cell membrane. The output data consist of spatial and temporal trajectories collected for many hundreds of individual molecules that are observed simultaneously. Further statistical analysis of these data sets enables binding kinetics and diffusion coefficients to be derived. Wide-field, camera-based, detection methods, using either cooled-CCD or image-intensified cameras combined with intense laser excitation of the specimen, enable detection of single fluorophores. The challenge is to detect their emission within the context of a living cell where autofluorescence and fluorescence from out-of-focus fluorophores is significant. Unlike camera noise, both of these sources of noise increase with excitation power (3). So, to obtain sufficient signal/noise, sources of background fluorescence must be minimized and the fluorophores must be present in the nanomolar (nM) concentration range. This gives an average of one fluorophore per cubic micron and if an optical sectioning technique is used, individual fluorophores then appear as spatially separated spots of light. The intensity distribution, or point spread function (PSF), of an individual fluorophore corresponds to an Airey disk pattern with a characteristic fullwidth at half-maximum height (FWHM) determined by the wavelength of light, λ, and numerical aperture, NA, of the imaging system (given by 0.6 λ/NA). The most widely used form of microscopy for single fluorophore studies is TIRFM (4). The non-propagating, or evanescent, field created by TIR illumination excites fluorophores only at the interface between the microscope coverslip and the aqueous medium, leaving the rest of the specimen unilluminated (1,5,6). This feature makes the method ideal for studying fluorophores present at the basal membrane of living cells or within thin membrane protrusions like the leading lamella (7).

In most studies published to date, records have been analyzed manually, frame by frame, to identify each individual fluorophore (8). Such manual detection methods are prone to observer bias and are simply impractical if many hundreds or thousands of individual fluorophores need to be identified and tracked in time. Here, we describe two algorithms (SFDA and ASPT) that automatically detect individual fluorophores in video recordings and output intensity and position data as a function of time (trajectories) giving a much reduced data set. Fluorophores exhibiting ''blinking'' behavior or unexpected fluctuations in fluorescence with time can be excluded from final analysis. To test our methodology we generated

Submitted January 12, 2006, and accepted for publication December 1, 2006.

Address reprint requests to G. I. Mashanov, E-mail: gmashan@nimr.mrc.ac.uk; or J. E. Molloy, Tel.: 44-0-208-816-2110; Fax: 44-0-208-906-4477; E-mail: jmolloy@nimr.mrc.ac.uk.

© 2007 by the Biophysical Society

0006-3495/07/03/2199/13 $2.00

doi: 10.1529/biophysj.106.081117

model data sets using a Monte Carlo based computer program that produced simulated video records with realistic levels of camera noise, single fluorophore emission rate, background fluorescence, and photobleaching. Model input parameters could be set from our experimentally determined values (below). This allowed us to cross-validate our algorithms since we knew a priori where and when ''single fluorophore'' signals were present in the data. We could then determine the proportion of false and missing events and this was important in validating our methodology. We also tested the algorithms using real imaging data obtained from control, in vitro, specimens and live mammalian cells.

We have measured the mobility of isolated pleckstrin homology (PH) domains and full-length PLC-δ1 at the plasma membrane of live mammalian cells. PH domains bind to phosphoinositide phosopholipids and serve to target proteins to membrane. The PH domain structure is highly variable between protein families but exhibits a conserved fold motif of seven β-strands that form a β-sandwich (three of the strands run orthogonal to the other four) and a single α-helix that caps one end of the structure. The target phospholipid headgroup is specified by variable loop regions that link the β-sheets and α-helix. Using eGFP fusion protein constructs we have investigated the membrane targeting and mobility of different types of PH domain. PH123 isolated from myosin-10 and full-length phospholipase C-δ1 (PLC-δ1), which is involved in activating cell signaling pathways by hydrolysis of the phosphatidylinositol-4,5-bisphosphate ($PI(4,5)P_2$) headgroup to release the active molecules inositol trisphosphate (IP_3) and diacyl glycerol (DAG). PLC-δ1 binds specifically to PIP(4,5) and its enzymatic activity is thought to be processive since multiple enzymatic turnovers arise from each diffusional encounter with membrane (9). PLC-δ1 might be expected to diffuse more slowly at regions of membrane that are rich in PIP(4,5) (see Balla et al. (10)), because lipid-lipid interactions and frequent encounters between lipid headgroups and enzyme would cause it to dwell within the ''raft'' of substrate. As the localized region of substrate became depleted the enzyme might then exhibit higher mobility. If so, then such behavior might be revealed by tracking the diffusive motions of individual molecules (11). In this study we compared the diffusive behavior of PLC-δ1 with that of PH domains (PH123) isolated from myosin-10.

MATERIALS AND METHODS

Single fluorophore control samples: in vitro experiments

For our control specimens we used a microscope flow-cell arrangement described previously (12). Briefly, we used a precleaned 25×72 mm^2 glass microscope slide across which two 3×22 mm^2 strips of (No.1) coverglass were fixed 10 mm apart using 2 μl of UV curing epoxy adhesive (RS components, Northants, UK). A 22×40 mm^2 precleaned coverslip was glued onto the coverglass strips, orthogonally to the slide, leaving ~10 mm of coverslip projecting from either side. The flow-cell was exposed to UV light until the glue was completely cured. This produced a central channel with height of 150 μm, length 25 mm, width 10 mm, volume of 50 μl, and surface area 500 mm^2. The flow-cell was mounted on the inverted microscope (see below) and solutions could be added and removed at the projecting pieces of coverslip either side of the flow channel. The flow-cell was filled with phosphate buffered saline (PBS) solution (pH 7.4) containing 5 μg/ml (33 nM) polyclonal anti-GFP antibodies (Abcam, Cambridge, UK). The 50-μl volume of solution used would therefore contain ~10^{12} molecules, this would provide 2000 molecules/μm^2 if all of the antibodies bound to the surface. This solution was left to incubate in the flow-cell for 5 min and after few washes with PBS the solution was replaced with the same buffer containing 0.2–20 ng/ml (i.e., up to 0.74 nM) eGFP (Clontech, Palo Alto, CA) for 5 min. Unbound protein was then washed out of the flow-cell by several washes with PBS. If all of the GFP molecules bound to the glass surface then, at the highest concentrations used, this would give 45 molecules/μm^2.

Single fluorophore observations in living cells: in vivo experiments

To study live cells by TIRFM we used cultured human umbilical vein endothelial cells (HUVECs) (gift of Dr. T. Carter, NIMR, London, UK), primary mouse myoblasts (gift of Dr. M. Peckham, University of Leeds, UK), and 3T3 mouse fibroblasts. Cells were transfected with the eGFP fusion protein constructs (below) using Genejuice (Novagen, Merck Biosciences, Nottingham, UK) following the recommended protocol (7). After 24 h, the cells were replated onto round coverslips (Ø = 25mm) and allowed to settle. Eight hours later, the medium was replaced with Hank's balanced salt solution containing 20 mM HEPES (pH 7.4) (Sigma-Aldrich, Poole Dorset, UK), and the coverslip was then assembled into a circular, stainless steel, imaging chamber that held two round coverslips separated by a silicone O-ring (Ø = 2.5 mm, 25 mm outer diameter). The imaging chamber was filled with Hank's balanced salt solution containing 10% of fetal calf serum (Sigma-Aldrich), and the assembly was then mounted on the microscope. The microscope (see below) was enclosed in a temperature-controlled Perspex box (Solent Scientific, Segensworth, UK) and Peltier cooling elements were used to cool the objective lens and imaging chamber (RS components, Northants, UK). We found that ~10% of the cells had a suitable level of expression for TIRF measurements such that single molecules could be visualized as isolated, single spots. We examined recombinant PH domains from myosin-10 (7) and PLC-δ1 that had been fused, in-frame, with eGFP. Both molecules possess PH domains that become targeted to the phosphoinositide phospholipids in the plasma membrane. They bound tightly to the plasma membrane of mouse myoblasts and showed only very slow lateral diffusion whereas in fibroblasts and HUVECs the proteins exhibited much higher mobility.

Single fluorophore imaging: TIRFM

The TIRFM system used for imaging is based around a Zeiss Axiovert 135 inverted microscope (Carl Zeiss, Welwyn Garden City, UK) described earlier (13). Briefly: a blue laser beam (488 nm, 20 mW, Protera 488, Novalux, Sunnyvale, CA) was expanded using a Galilean beam expander to give the correct numerical aperture (far-field beam diameter of ~8 mm. The laser light was focused, using a 160-mm focal length lens, at the back focal plane of a high numerical aperture objective lens (AlphaPlan, 100×, NA 1.45, Zeiss, Jena, Germany). A front-surface, silvered, mirror (Ø = 3mm) was used to direct the laser beam into the objective lens by positioning it immediately below and at the extreme edge of the back aperture. An identical mirror, placed on the opposite side of the back aperture was used to direct the laser beam out of the microscope as it was reflected back by the TIR effect. The average laser intensity at the specimen plane was ~10 μW/μm^2. Images were collected using an image-intensified, CCD camera (GemStar, Photonic Science, Robertsbridge, UK). Sequences of images (records) were stored directly to computer hard drive for later analysis. Throughout, intensity data

refer to digital counts scored by our camera system. Imaging software was written using C++ language (Borland CBuilder6, Scotts Valley, CA).

Description of SFDA and ASPT algorithms

To study the properties of membrane-bound proteins inside living cells we devised two single fluorophore detection algorithms. Our aim has been to minimize observer bias and enable large, single-molecule data sets to be collected so that subsequent statistical analysis can be performed. In this section, we describe the analytical tools that were developed and then show how they were tested against experimental data sets obtained from in vitro and live-cell imaging studies (see Appendix for detailed description of the methods).

Single fluorophore detection algorithm

The single fluorophore detection algorithm is based on three characteristics of single fluorophores: A), diffraction-limited size; B), known and constant emission rate; and C), abrupt, single-step photobleaching. Single fluorophore data sets are inherently noisy so the first stage of our detection algorithm consists of spatial and temporal filtering designed to reduce the known noise properties while retaining single fluorophore signals. The next phase of the SFDA is to separate signals arising from single fluorophores from noise. Single fluorophores emit a steady number of photons per second under constant illumination before suddenly and irreversibly photobleaching. So, we expect the signal to exhibit a stepwise drop in intensity to background level that is correlated among neighboring pixels (Fig. 1). Provided the fluorophore does not move in the *x-y* plane during data collection, then a temporal ''edge detection'' algorithm can be used to automate identification of such events within a sequence of video data. The derivative of the intensity data is computed using suitable weightings and window size (e.g., Prewitt or Sobel filters), extreme values (most positive and negative) for each pixel location and the time at which the transitions occurred within the video record are stored in so-called, ''drop mask'' and ''rise mask'' data arrays. When these arrays are displayed as a pseudocolor image the position of individual fluorophores appear as bright spots and individual *x,y* centroids can then be calculated for each individual fluorophore using information stored in the mask arrays to extract the original, time-series, intensity data from the correct section of video. Individual fluorophore centroid positions are determined by a Gaussian fitting procedure that gives a resolution of ~40 nm (limited by the number of photon counts per fluorophore image) (14). At this point in the analysis a check is also made that the size and intensity of the putative fluorophore conforms to the expected criteria (see A

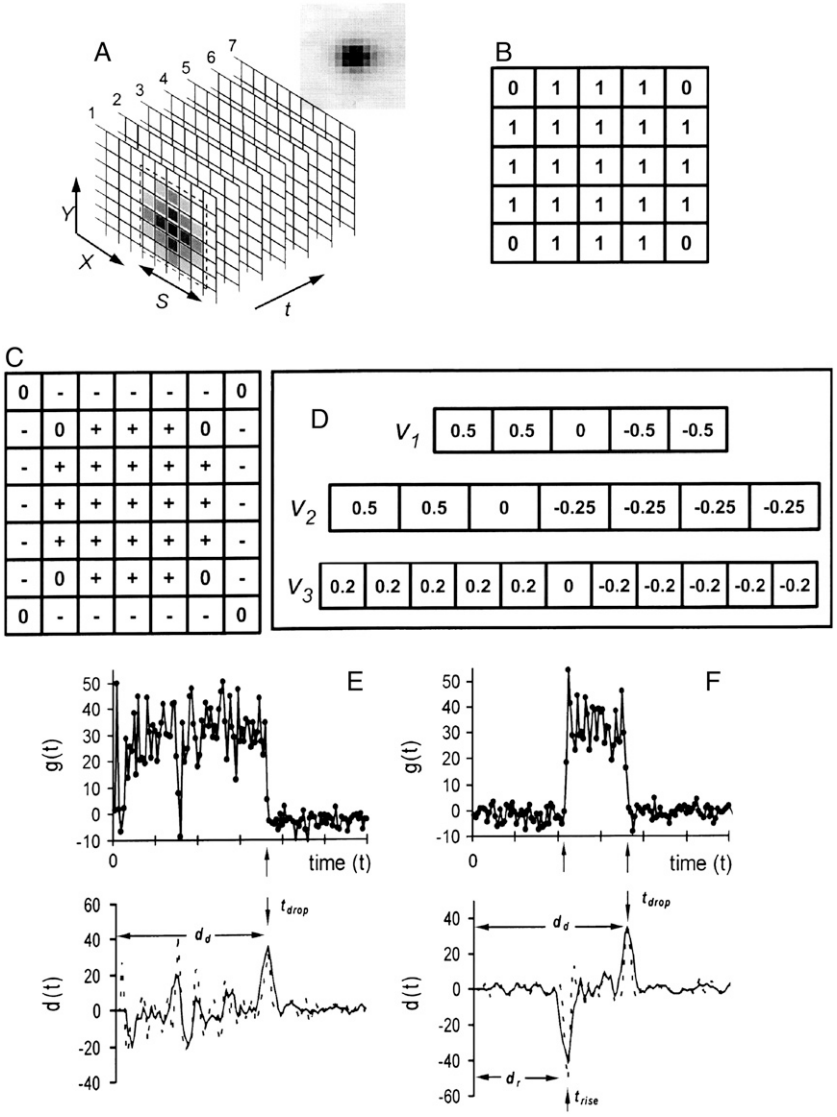

FIGURE 1 Single fluorophore detection algorithm. (*A*) Raw image data consist of a stack of *x,y* pixilated images with a third dimension, *t*, of time. Individual pixels represent the fluorescence intensity $f(x,y,t)$. Each single fluorophore image (*inset*) spreads over a number of pixels and intensity needs to be integrated over this area, *S*. (*B*) A moving kernel is used to find the average intensity over an area, *S*, giving a low-pass filtered image, $g(x,y)$. (*C*) The kernel can be expanded to include a peripheral region, S', with negative weightings to give local background correction. (*D*) The first derivative in time, $d(x,y,t')$, of $g(x,y,t)$ array is computed using a Sobel or Prewitt filter, $v(t)$, of length *L*. (*E*, *upper*) The fluorescence intensity $g(x,y,t)$ of an eGFP molecule present from the beginning of the record produces a first derivative signal, $d(x,y,t')$, (*lower panel*) using the kernal $v(t)$ of form, $v3$ (*solid line*) or $v1$ (*dashed line*). (*F*, *upper*) eGFP arrived during the record; the lower panel again shows the first derivative $d(x,y,t')$ calculated by moving the kernel $v(t)$ through the data; $v3$ (*solid line*), $v1$ (*dashed line*).

and B above). A problem encountered in live-cell imaging experiments is that background fluorescent material and cell autofluorescence produce short-lived ''false'' events that contribute unwanted noise to the mask arrays. When short-lived events (duration $< t_{min}$) were excluded, a proportion of ''real'' (but short-lived) events were also excluded. The number of missing real events erroneously excluded in this way can be estimated by extrapolating the lifetime distribution plots obtained from analysis of the long-lived events, which we detect with more certainty, or alternatively by analysis of simulated or modeled data sets (see below) in which we know, a priori, the noise and signal components. Sole reliance on simulated data to test the analytical approaches leads to circularity in the arguments, so we used both simulated and experimental data sets to test the procedures.

The final part of the SFDA algorithm is to output information about all detected objects including; fluorescence intensity, timing, and *x-y* coordinates. These data are stored in a format suitable for further analysis in statistical packages or Excel spreadsheets.

Automatic single particle tracking

Automated single particle tracking presents a different set of problems to detection of static fluorophores (i.e., the SFDA method). The filtering and statistical tests need to be modified to allow intensities to be tracked in space and time. To track individual fluorophores at the plasma membrane of living cells, video data must be acquired at high speed. This is because the lateral diffusion coefficient (D_{lat}) of a protein in membrane is large compared to the PSF of the fluorophore and its image is therefore smeared out (or blurred) by its diffusive motions. For instance if $D_{lat} = 0.5\ \mu m^2/s$ then there will be ~1.4 μm movement within 1 s. Here, we assume that raw data are collected at sufficient speed that fluorophore movement during individual video frames is small compared to the idealized PSF measured in control, fixed samples (above). Our ASPT algorithm identifies locations of putative single fluorophores within the video record then tracks their positions between consecutive video frames. The first phase works by pattern-matching regions of the image to the known PSF of a single fluorophore (Fig. 2). Idealized fluorophore centroids are then stored as an array of *x,y,t* locations. The second phase of the ASPT routine links object coordinates between adjacent video frames using a nearest-neighbor algorithm. If the tracked objects move close to each other (~FWHM) and their images coalesce, then if the resulting image deviates significantly from the idealized single fluorophore PSF, both tracks will be terminated. However, if the resulting image approximates that of a single fluorophore then only one track is terminated. Once the object tracks have been identified, the original intensity data are used to refine our estimate of the fluorophore centroids with subpixel resolution (as for SFDA above). Finally, to discriminate single fluorophores from multifluorophore clusters the original intensity data can be inspected to ensure that each object exhibits single-step appearance and disappearance (photobleaching) and has an average intensity similar to that of known single fluorophores measured in our in vitro control specimens.

Simulated/modeled data sets

To test the analytical routines, simulated data sets were created that closely resemble real experimental data in terms of noise levels and fluorophore behaviors. Simulated data allow synthesis of different signal/noise ratios and certain knowledge of modeled fluorophore locations. This might appear to be a circular solution to the problem, i.e., using simulated data to test the analysis tools. However, use of simulated data enables testing of complex, nonlinear problems, e.g., discontinuities associated with limited kernel sizes and thresholding methods, both of which greatly speed up computation time but introduce nonlinearities by creating boundary conditions. The combined effects of all these potential problems can be tested and quantified, in an empirical way, using simulated data sets.

We modeled individual fluorophores as Gaussian intensity PSFs in which images were created with the correct photon noise characteristics. We used a Box-Muller algorithm (adapted from Press et al. (15)) to generate random *x-y* coordinates for each modeled photon within the PSF. We also added Gaussian noise to every pixel to mimic our camera characteristics (RMS amplitude δ). The signal/noise ratio (SNR) was defined as mean fluorophore intensity divided by the sum of RMS background noise and RMS signal shot noise (16). All parameters, including fluorophore position and intensity could be controlled for every video frame that was generated. Modeled fluorophores were either static or were allowed to move in the *x-y* plane assuming a simple random-walk behavior.

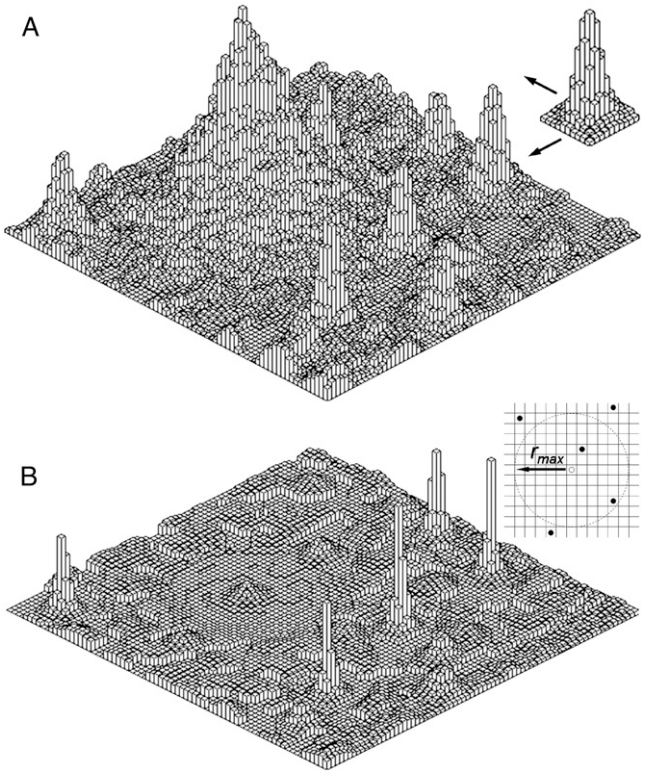

FIGURE 2 The core operation enabling automatic single particle tracking involves measuring the inverse variance of the raw image data with respect to an idealized point spread function for a single fluorophore. The upper panel (*A*) shows typical raw image data obtained for single GFP-tagged proteins expressed at low levels in a myoblast cell. Note the large patch of fluorescence, upper left part of the image. The convolution kernel is shown in the inset (*right*). In the lower panel (*B*) the output data following the mathematical operation (Eq. 8) are shown. Note that regions of intensity that form a good match to the idealized single fluorophore PSF are reinforced whereas others are not. Nearest-neighbor algorithm (*inset*) can be used to link objects appearing on consecutive images. See Appendix for explanation.

RESULTS AND ALGORTHM TESTING

In this section, we deal first with analysis of our model data sets (described above) then results from our in vitro control experiments, using eGFP immobilized on GFP antibodies. Finally, we present data from live cell imaging of cultured myoblasts, fibroblasts, and HUVECs, each expressing eGFP-tagged PH domains from either myosin-10 or full-length PLC-δ1.

Testing the SFDA algorithm using simulated data sets

To test the SFDA on image sequences generated by the model described above, 1000 simulated fluorophores were uniformly distributed across the image plane at 2 μm intervals (Fig. 3 *A*). Background noise level was increased systematically to give SNR from 4.5 to 1.6 (16,17). Simulated data sets were analyzed using the SFDA software and the number of ''real'' and ''false'' events detected at each signal/noise and three detection threshold values ($I = 1, I = 1.5, I = 2$) were plotted (Fig. 3 *B*). At $SNR = 2.2$, and high detection threshold value ($I = 1.5$) 37% of the real events were detected and 3% false events were generated. However, when the detection threshold was lowered ($I = 1$) 80% of the real events were scored but there was an unacceptably high level of false events (36%). Under all conditions, dwell time histograms gave a reliable estimate of the photobleaching rate constant (Fig. 3 *A*, *lower*). We found our real experimental data sets (see below) have a SNR between 2.5 and 4 and when we tested the SFDA using SNR in this range we detected >95% of the real events and generated <1% false events. The runtime was 66 s for 200 images, 745 × 863 pixels, using a Pentium-IV-3.2 GHz, with 2 Gb RAM) i.e., ~5× slower than ''real time''.

Testing the ASPT algorithm using simulated data sets

The ASPT algorithm was tested using the same image sequences generated for SFDA testing (see previous section and Fig. 3, *A* and *B*, for details). At $SNR = 3.3$, we detected

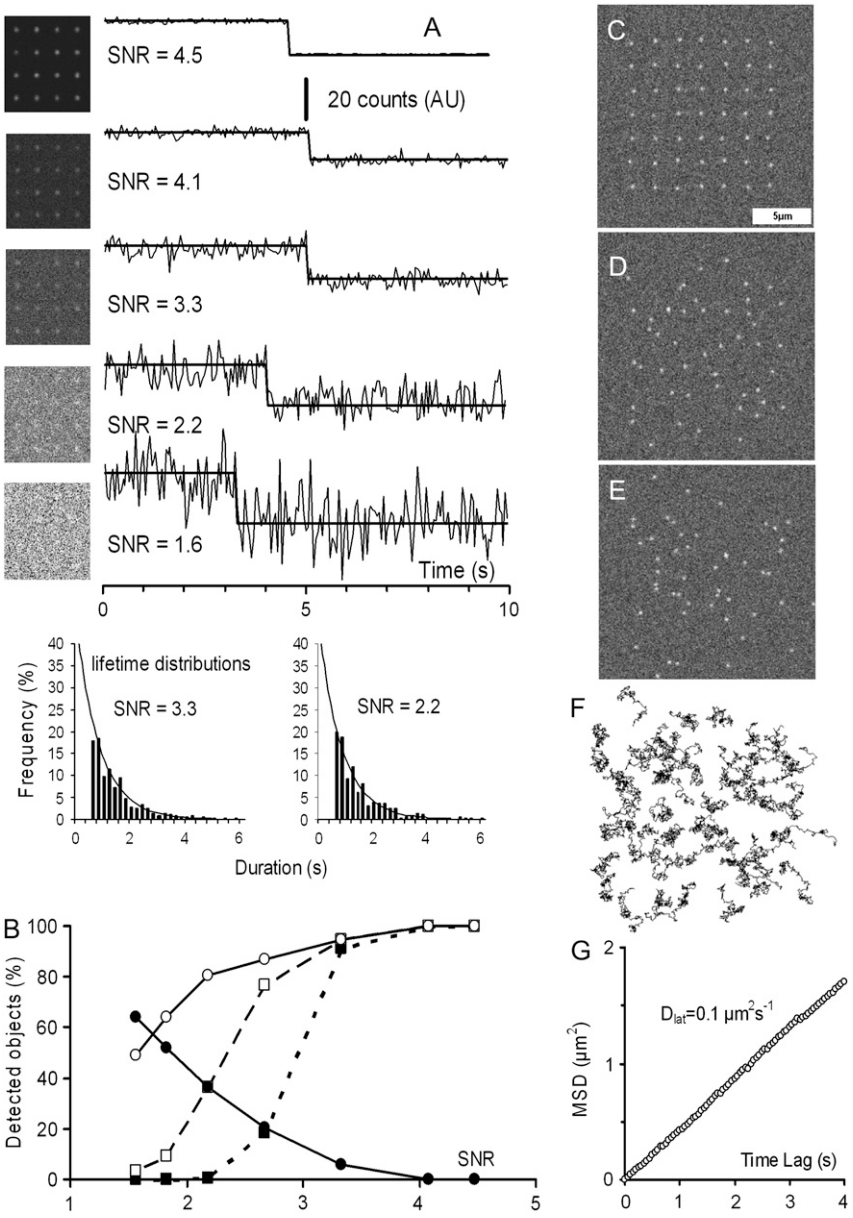

FIGURE 3 To test the SFDA routine, simulated data sets were created in which; average fluorophore emission rate is 10,000 photons/s (500 photons/PSF/frame), FWHM is 250 nm, photobleaching rate 1 s^{-1}, imaging rate 20 frames/s. Background noise was systematically increased from 1 to 60 counts (RMS) per pixel per frame (pixel size 85 × 85 nm). (*A*, *left panel*, *images*) Data obtained in our TIRF experiments for in vitro and live-cell imaging resembles the simulated images with RMS noise of ~10–40 counts/pixel/frame (SNR = 2–4). (*A*, *graphs*) Intensity versus time plots closely resemble our experimental data sets. The lifetime distributions extracted from the SFDA analysis at different SNR (*A*, *lower*) were fitted by a single exponential distribution. To estimate the mean event lifetime the threshold, t_{min}, (here set at 0.5 s; note missing bins below this value) must be subtracted from the calculated mean of the scored data (i.e., true mean = mean − t_{min}). The model value was 1 s and the values from SFDA were 1.03 s at $SNR = 3.3$ and 1.01 s at $SNR = 2.2$. (*B*) The rate of event detection and false event generation using the SFDA algorithm was measured using different threshold levels (parameter *I*, see Appendix for details) as a function of SNR levels. (○) Proportion of real events detected (threshold, $I = 1$); (●) false events generated expressed as proportion of the total number of real events ($I = 1$); (□) proportion of real events detected at $I = 1.5$; (■) proportion of real events detected at $I = 2.0$. To test the ASPT routine, simulated fluorophores were allowed to move randomly with $D_{lat} = 0.1\ \mu m^2\ s^{-1}$; a total of 49 fluorophores were simulated with $SNR = 4$. Images are shown at $t = 0$, $t = 5$ s, and $t = 10$ s (panels *C–E*). ASPT with threshold $Q_{min} = 0.2$ (Eq. 8), $r_{max} = 430$ nm, and $n_{min} = 10$ was used to track these objects. Panel *F* shows resultant tracks generated by the ASPT analysis. Note 77 tracks were generated from 49 fluorescent objects as broken tracks arise when images overlap or noise prevents tracking an individual object. (*G*) Averaged MSD versus time lag plot was used to calculate D_{lat} for fluorophores detected in panel *F*. The value was correct to within 1% of the input model value. Scale bar is 5 μm.

71% real events and generated 23% false events. At lower signal/noise ratios ($SNR = 1.8$), we detected 16% real events and but generated 18% false events. Dwell-time analysis of our scored events revealed a systematic overestimation of the photobleaching rate, 4 s^{-1} (actual value = 1 s^{-1}) at low SNR. At high SNR values ($SNR = 3.3$) the estimated rate was 1.1 s^{-1}, and much closer to the true value. Analysis runtime was 129 min (at $SNR = 1.8$), which is 100 times slower than the SFDA procedure.

To test ability of the ASPT routine to track fluorophores we used the same model as above but without photobleaching and allowed simulated fluorophores to move randomly in the *x-y* plane (see Fig. 3, *C–E*) with a $D_{lat} = 0.1$ μm^2 $s.^{-1}$ Analysis of the records by ASPT at $SNR = 3.3$, was followed by a least-square fit to the mean-square displacements (MSD) versus time lag (δt), which gave an estimate for $D_{lat} = 0.101$ μm^2 s^{-1} (see Fig. 3 *G*). However, at lower $SNR = 2.2$, several tracks could be generated for the same object. We found that a multitude of short tracks arises because each time the fluorescence signal dropped below the detection threshold its track was prematurely terminated. When fluorescence reached the level above threshold in a subsequent image it initiated a new track apparently belonging to the same object. This problem does not affect estimates of the diffusion coefficient but does lead to a systematic underestimation of the fluorophore lifetime.

In vitro experimental control specimens

To measure the signal-and-noise levels of our TIRFM imaging system, eGFP was immobilized via anti-GFP antibody to microscope coverslips at very low surface density. At high laser excitation power, individual fluorescent objects were clearly visible in the video images. Plots of raw intensity data from background regions of interest compared to regions (spots) of high intensity plotted as a function of time show clear single-step photobleaching behavior (Fig. 4 *A*). A histogram of the raw intensity data shows that background noise and single fluorophore emission are readily discriminated (Fig. 4 *A*). The SFDA and ASPT algorithm both reliably detect individual fluorophores under these conditions. However, it is critical to ensure that the intensities being measured arise from single fluorophores and not clusters of multiple molecules. To ensure that the single fluorescent objects observed arise from an individual fluorophore we made serial dilutions of eGFP and measured how the number of detected fluorescent spots per unit area varied as a function of the concentration of applied eGFP in the bulk solution (Fig. 4 *B*). The average SNR for eGFP bound to glass was 2.4.

Knowing the volume of solution, the concentration of eGFP and the surface area of the microscope flow cell, the expected surface density of bound eGFP molecules could be calculated. By plotting the number of spots detected by SFDA or ASPT against the expected number we could then determine if just a single molecule was required for each event scored by measuring the limiting gradient of the plot at low surface densities. A log-log plot shows that the limiting gradient is unity indicating that, at low surface densities, each detected object corresponds to a single eGFP (Fig. 4 *B*).

Using the SFDA to analyze video data recorded over many hundreds of seconds we could also measure the rate at which the fluorescent spots (eGFP) bound to the antibody-coated glass surface. Each new object that appeared at the surface was scored so that the cumulative total number of objects could be plotted against time. This allows the

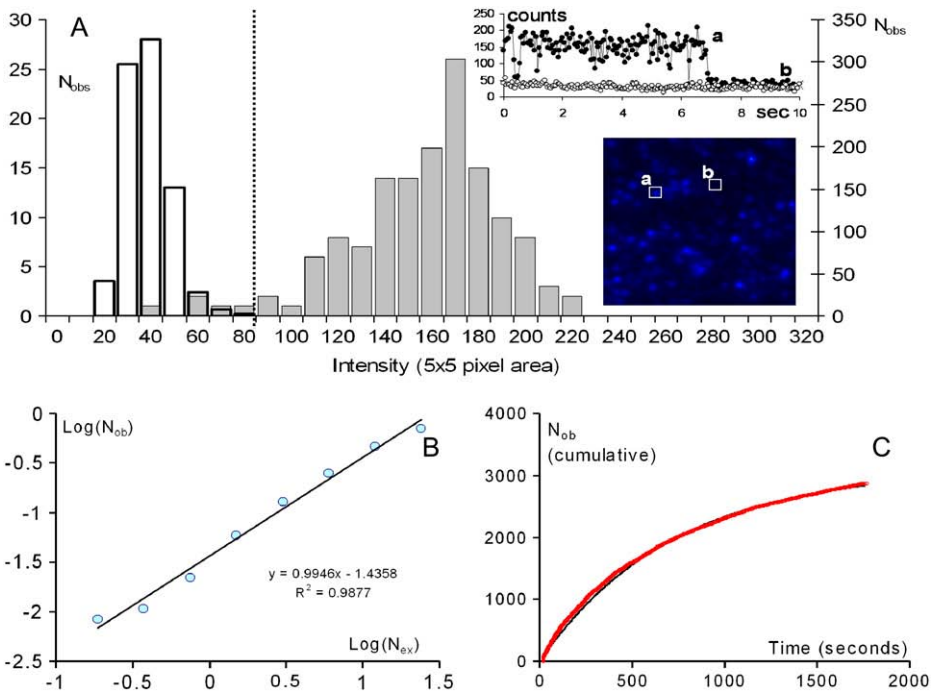

FIGURE 4 (*A*) Individual spots of fluorescence intensity caused by eGFP bound to antibody were viewed by TIRFM (shown as the *inset* image). Regions of interest (labeled *a* and *b*) representing high and low fluorescence areas were identified and the intensity versus time was plotted (*upper graph*, showing intensity versus time). A histogram of the intensity distribution measured over the first 6 s shows that the fluorescent spot could be readily identified from background on the basis of simple thresholding. We found that both the SFDA and ASPT algorithms (described in the text) were able to readily discriminate the fluorescent objects from background in images with such high signal/noise ratio. (*B*) To ensure individual molecules were being detected we made a log-log plot of number of spots observed against number predicted based on the dilution factor. The limiting gradient was unity. (*C*) The rate of eGFP binding to the antibody coated surface was measured by plotting the cumulative score of the arrival of each new fluorescent spot with time.

accumulation of new molecules binding at the surface to be followed in time giving a half-time to saturation binding, using our flow-cell arrangement, of 700 s (Fig. 4 *C*).

Detection of single fluorophores in vivo

We used the same instrument settings (camera gain; laser power and so on) as above to study the mobility of eGFP-tagged PH domains in live cultured mammalian cells. Using the procedures described earlier, we viewed individual, transfected cells adhered to glass coverslips using our TIR microscope. In our initial observations, we found that mobility depended greatly upon the cell type used; in mouse myoblasts, PH domains showed very low mobility (Fig. 5), whereas in 3T3 fibroblasts (Fig. 6, *A* and *C*) and HUVECs (Fig. 6 *H*) they were much more mobile (fitted $D_{lat} = 0.17\ \mu m^2\ s^{-1}$ for HUVECs). Also, we found that transfection of the primary myoblasts was much less reproducible in terms of expression levels and so it was difficult to obtain data sets from different cells under different conditions. So, here we report studies of different PH domains expressed in HUVECs and 3T3 fibroblast cell types.

We visualized individual eGFP-tagged PLC-δ1 bound in at the plasma membrane of fibroblasts at 23°C (Fig. 6 *A*). Individual fluorescent spots were highly mobile and we used the ASPT analysis to detect and track individual fluorophores (Fig. 6 *C*). To compare results obtained with ASPT and SFDA analysis on the same sample we cooled the cells to 3°C to inhibit the lateral mobility (Fig. 6, *B*, *D*, and *F*, *inset*). We found that under these conditions mobility was reduced by a much greater extent than expected from the change in absolute temperature (e.g., from 296 to 276 K)(18). We used both ASPT and SFDA to detect single fluorophores (Fig. 6, *D* and *F*) and found that ability to detect single fluorophores was similar but the average duration of measured events was shorter using ASPT. The apparent ''off rate'' was 4.5 s^{-1} using ASPT, compared to 2 s^{-1} using SFDA (Fig. 6 *F*). Note that under the illumination conditions used in these experiments, the rates are dominated by photobleaching rather than dissociation or unbinding from the membrane.

We then measured the mobility of PLC-δ1 and PH123 in fibroblasts and HUVECs and found that the rate of diffusion was higher in HUVECs than in fibroblasts (see Table 1). Also, PLC-δ1 diffused faster than PH123 except at long time intervals in HUVECs (Fig. 6, *G* and *H*) where we discovered very restricted mobility of PLC-δ1. Plots of MSD versus δt show that the apparent diffusion coefficient, proportional to

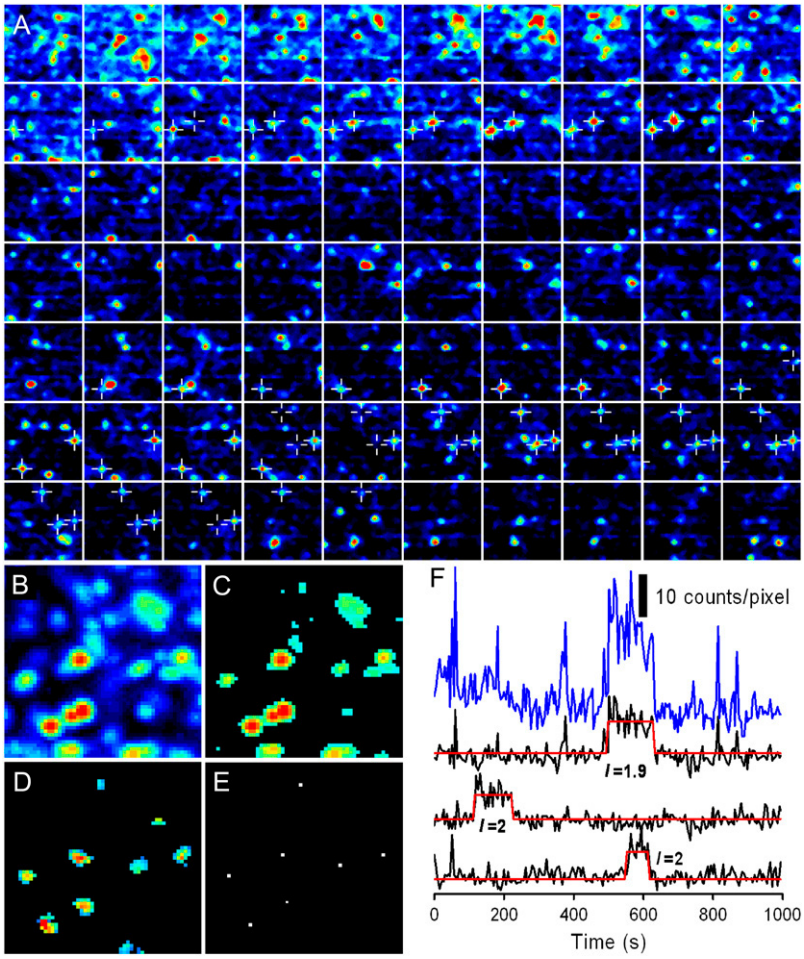

FIGURE 5 SFDA algorithm was used to detect individual eGFP-tagged PH123 molecules on myoblast plasma membrane (TIRF microscopy, time-lapse mode, imaging rate 0.2 s^{-1}). (*A*) A sequence of 70 images, 6 × 6 μm^2 shows small region of the cell membrane. Individual eGFP-PH123 molecules appear at the membrane as isolated spots of light. Molecules stayed attached at the same position, sometimes for hundreds of seconds, and suddenly disappear due to dissociation or photobleaching. Crosshairs show positions of the detected fluorophores when they were present on image. (*B*) Shows a pseudocolor image (*blue-yellow-red* palette) representing ''drop'' + ''rise'' mask image (see SFDA description for details). (*C*) The same as *B* but pixels that had values less than a threshold level (10 counts/pixel) were zeroed leaving bright isolated spots for future analysis. (*D*) This image contains *I* values (Eq. 6) calculated for every pixel selected in *C*. (*E*) Local maximum finding was used to calculate fluorophore position with pixel or subpixel resolution. (*F*) Fluorescence intensity tracks of three eGFP-PH123 molecules detected on record shown in panel *A*. Kernels (see Fig. 1, *C* and *D*) of type, v_3, were used for detection. Blue graph (*upper trace*) shows the intensity of a single central pixel (of the trace immediately below) and the three lower traces show average intensity for three spots measured over area, *S*, plotted against time (see legend to Fig. 1 and Appendix).

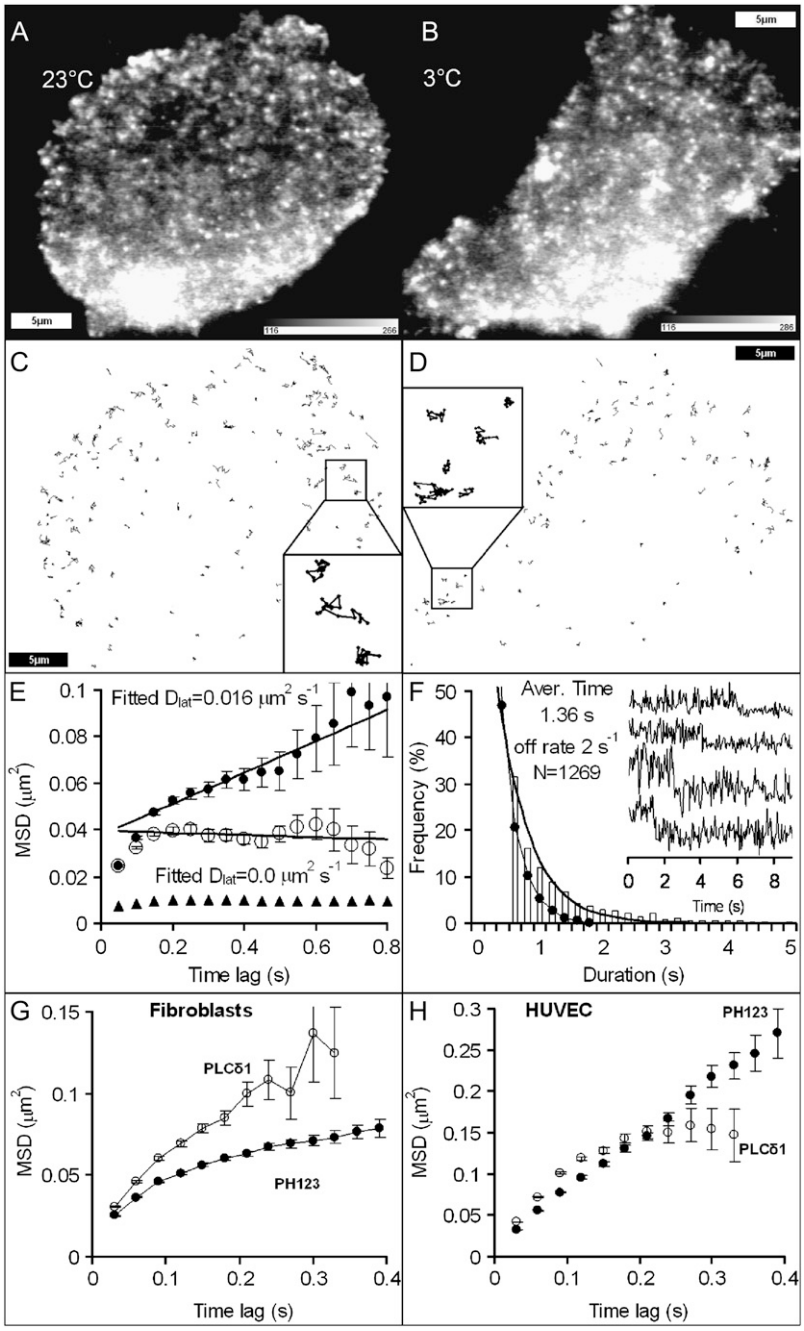

FIGURE 6 SFDA and ASPT algorithms were used to detect and track individual eGFP-tagged PLC-δ1 molecules at 3T3 fibroblast plasma membrane (TIRF microscopy, imaging rate 20 s^{-1}). (*A*) An averaged image of the first 10 images captured at the beginning of the record made at 23°C. (*B*) An averaged image of the first 10 images captured at the beginning of the record made at 3°C. (*C*) ASPT algorithm was used to track individual eGFP-PLC-δ1 molecules moving on basal membrane of the cell shown in *A*. Inset shows tracks in magnified region, 3 × 3 μm^2. (*D*) ASPT with the same parameters ($Q_{min} = 1.2$, $r_{max} = 5$, $n_{min} = 10$) was used to track individual eGFP-PLC-δ1 molecules moving at the basal membrane of the cell shown on *B*. Inset shows tracks in magnified region, 3 × 3 μm^2. (*E*) Averaged MSD versus time lag (δt) plot was used to calculate D_{lat} for eGFP-PLC-δ1 at 23°C (*solid circles*) and at 3°C (*open circles*). Control studies, in which eGFP was bound to the coverslip via antibodies, gave an estimate of positional noise under optimal imaging conditions (*triangles*, see Fig. 4 for details) root MSD = 75 nm. Although the same imaging conditions were used in the live cell studies, SNR was lower because of background fluorescence. Consequently, accuracy of tracking of eGFP-PLC-δ1 in fibroblasts at 3°C gives a higher noise level root MSD = 200 nm. (*F*) SFDA and ASPT algorithms were cross-validated on data obtained with eGFP-PLC-δ1 in fibroblasts at 3°C. The number of detected molecules was similar ($n = 1259$) but the ''off'' rate using ASPT was faster (*solid circles* with fit to *dotted line* = 4.5 s^{-1}) than that measured by SFDA (*bars* with fit to *solid line* = 2 s^{-1}). (*G*) eGFP-PLC-δ1 (*open circles*, three cells, $n = 1396$) and eGFP-PH123 (*solid circles*, 15 cells, $n = 7381$) molecules were tracked in fibroblasts at 23°C, imaging rate was 33 s^{-1} and MSD plotted as a function of time lag (δt) between data points. (*H*) The study was repeated using eGFP-PLC-δ1 (*open circles*, 15 cells, $n = 5022$) and PH123 (*solid circles*, 12 cells, $n = 2803$) in HUVECs. MSD versus δt plots indicated both proteins moved with random-walk behavior in 3T3 fibroblasts. However PLC-δ1 in HUVECs showed anomalous subdiffusion, or restricted diffusion with an apparent compartment size of 0.7 μm (given by $(3MSD)^{0.5}$).

the gradient of the graph, is high over short timescales but low over longer timescales. This nonlinearity is particularly evident at 23°C (Fig. 6 *H*). This phenomenon, known as anomalous subdiffusion, is well described in the literature (19) and indicates that PLC-δ1 undergoes restricted diffusion at the plasma membrane in HUVECs.

DISCUSSION

Two digital image processing methods, SFDA and ASPT, have been described that enable automatic detection of individual fluorophores within live cell and in vitro experiments using TIRF microscopy. We developed a statistical test (see Appendix for details) that helps separate single fluorophore events from background noise and checked our algorithms using modeled data, in vitro control specimens, and data from live cell imaging experiments. Depending upon the cell type used and experimental temperature the eGFP-tagged proteins were either static or highly mobile.

Computing the first derivative of intensity with time over pixel areas that cover 90% of the PSF gives a reliable means to detect characteristic, stepwise photobleaching of single

TABLE 1 Estimates of lateral diffusion coefficients derived from MSD versus δt plots around different time lag points

	Dlat $\mu m^2/s$ ($\delta t = 0.15$ s)	Dlat $\mu m^2/s$ ($\delta t = 0.3$ s)
PLC-δ1 in fibroblast 3T3	0.131 ± 0.005 (485)	0.114 ± 0.018 (50)
PH123 in fibroblast 3T3	0.094 ± 0.002 (3263)	0.059 ± 0.002 (645)
PLC-δ1 in HUVEC	0.212 ± 0.003 (1279)	0.128 ± 0.016 (100)
PH123 in HUVEC	0.187 ± 0.004 (998)	0.182 ± 0.011 (114)

Values were determined from the local gradients of graphs shown in Fig. 6, *G* and *H*, around the stated δt values given as mean ± SE (*n*) (measured at 23°C).

fluorophores in video data (SFDA core). The method exploits a combination of single fluorophore image attributes; A), their diffraction limited size; B), intensity remains steady until sudden photobleaching; C), or intensity suddenly increases and then remains steady (sudden appearance); and D), intensity matches known value that is measured in control studies.

The multipass nature of the SFDA algorithm presented here dramatically reduces computation time because background regions of the image are discarded at an early phase and the more time-consuming analysis is restricted to a much smaller data set. Furthermore, because our analysis moves between the processed data (masks) and original raw data we retain all possible detail that might be present in the raw data and can inspect the processed output by superimposing it upon the original video images. For example this allows detection of double or triple photobleaching events and subsequent partitioning of the data into single, double, or triple fluorophores.

The methodology was tested using simulated data and also experimental specimens in which single fluorophores were attached to microscope coverslips in a controlled fashion. Experimental samples, in which eGFP was immobilized to a glass coverslip using antibodies, showed that single fluorophores can be detected reliably. Simulated data sets that closely mimic these experiments enabled the true detection rate and false positive rate to be quantified. Simulated data sets were generated with a range of SNR that extend below and beyond the SNR of our experimental data sets.

Most automatic single particle detection and localization algorithms that have been described earlier (20–22) rely on multistage pattern recognition algorithms to identify and track diffraction-limited fluorescent spots with subpixel resolution (similar to the ASPT algorithm presented here). The published approaches require a SNR >5 whereas single fluorophores in live cells usually give a SNR approximately threefold lower than this. The ASPT algorithm, validated under realistic SNR, gave reliable detection and tracking of single fluorophores but tended to underestimate photobleaching rate. There are two factors: first, when two or more fluorophores move close together their tracks and object lifetimes are terminated. Second, noise can cause an object to be lost and this will also result in premature track termination. Both factors cause lifetimes to be systematically underestimated (i.e., off rate overestimated). The ASPT works well at low SNR because it uses the additional criteria that single fluorophores have constant and known level of fluorescence and this improves discrimination between single fluorophores and background noise. The ASPT algorithm suffers from a common problem (reported by other workers) in terms of deconvolving signals arising from overlapping point spread functions (i.e., when fluorophore separation approaches the Raleigh limit). However, by adjusting the imaging and experimental conditions, ASPT can be used to detect and track hundreds of single molecules within a single cell simultaneously. The positional resolution (i.e., the ±SE in estimating the mean position) depends upon the SNR ratio, microscope mechanical drift and, under ideal imaging conditions, is proportional to the square root of the total number of photons collected. Positional noise under the imaging conditions used for our live cell imaging (e.g., 33 frames per second) is 70 nm for eGFP bound via antibody to a coverslip and 200 nm for eGFP-PLC-δ bound to membrane at 3°C (see Fig. 6 *E*). Previous reports give positional resolution for detecting protein labeled with multiple cy5 fluorophores in the membrane of Jurkat cells of 40 nm (23).

Our studies of different cell types that transiently express eGFP-tagged PLC-δ1 and PH123 revealed different behaviors: First, mobility of both PLC-δ1 and PH123 was very different in the different cell types studied; PH123 domains in mouse myoblasts were practically immobile ($D_{lat} < 0.005$ $\mu m^2/s$) whereas in fibroblasts and HUVECs they exhibited higher mobility (Table 1). This implies that in myoblasts either the membrane viscosity is high or there must be other barriers to free diffusion at the membrane.

We found that when temperature was reduced from 23°C to 3°C lateral mobility of PLC-δ1 in fibroblasts was greatly inhibited. Such dependence of lipid mobility on temperature has been reported previously and has been proposed to be due to a liquid-gel transition (24). The phenomenon conveniently allowed us to cross-validate our two algorithms (ASPT and SFDA) within the same specimen.

The most striking result was that whereas PH123 domains showed unrestricted diffusion in HUVECs the diffusive motion of PLC-δ1 was anomalous. Nonlinearity in the MSD versus δt plots observed for PLC-δ1 can be explained in a variety of ways: 1), physical confinement by cytoskeletal proteins that act as mechanical barriers; 2), by presence of different lipid phases (lipid rafts); 3), by protein crowding or transient complexation (19). All of these physical models result in rapid diffusion on short timescales but slower diffusion on longer timescales. If we first assume the confinement model then the average size of the confinement region can be estimated from the position of the inflection in the MSD versus δt plots and would be ~0.7 μm. (Fig. 6 *H*). The fact that we do not observe the same phenomenon with PH123 domains might be because they are slightly smaller and therefore less likely to be hindered by cytoskeletal components.

However, the difference in molecular mass (eGFP-PLC-δ1 = 113,000 Da and eGFP-PH123 = 61,000 Da) indicates that the protein radii (proportional to $Mw^{0.33}$) would differ by just 20%. So we think it is unlikely that restricted diffusion of PLC-δ1 compared to free diffusion of PH123 can be explained solely by mechanical interactions between PLC-δ1 and cytoskeleton. Considering point 2 (above) it may be that PLC-δ1 and PH123 partition into different lipid phases. We know that PLC-δ1 binds tightly and specifically to ($PI(4,5)P_2$) whereas PH123 are more promiscuous binding to ($PI(3,4,5)P_3$) and ($PI(3,5)P_2$) (Dr. M. Peckham, University of Leeds, personal communication, 2002). There is evidence that ($PI(4,5)P_2$) lipid distributes nonuniformly (10) and regions rich in this lipid might therefore act as a raft structure to which PLC-δ1 associates whereas PH123 domains do not.

Finally, it has been proposed that PLC-δ1 interacts with membrane both by nonspecific electrostatic (weak) interactions (9) and by specific binding to the target $PI(4,5)P_2$ headgroup (25). When bound specifically to $PI(4,5)P_2$, mobility would be dominated by the lipid, whereas when bound by weak interactions much more rapid diffusive movements of the protein might occur. Kinetic studies of PLC-δ1 show that its enzymatic activity is greatly increased by phospholipid and mechanistically it can be considered a processive enzyme as it undergoes multiple enzymatic turnovers for each diffusional encounter with membrane (9). At the end of each catalytic cycle, PLC-δ1 will either proceed to hydrolyze another phosphoinositol headgroup or unbind and interact with the membrane weakly. However, simple modeling of this behavior shows that if the enzyme alternates between periods of fast and slow diffusion then a plot of MSD versus δt is linear with a gradient determined by the time-averaged value of the two diffusion coefficients. However, if there are localized regions of high $PI(4,5)P_2$ concentration (26) then the trajectory of PLC-δ1 might show low mobility within these regions (binding and unbinding at $PI(4,5)P_2$ molecules) and high mobility as it moves between patches localized to membrane by weak electrostatic interactions; this can lead to nonlinearity in MSD versus δt (27) and to transient variations in diffusion coefficient (11). We tested specifically for evidence of transient confinement of PLD-δ1 and also of PH123 using methods devised by earlier workers (28). To do this we ''stitched together'' all of the x,y coordinates from all of our molecular tracks (total $>$ 100,000 x,y pairs for PLC-δ1 and PH123) so that one molecular track followed on from the end point of the previous track. This enabled us to test for transient confinements either for an individual molecule within the data set or for periods of time within an individual molecular track. However, we found no statistically significant changes in diffusive motion (as defined by Simson et al. (28)) and the pooled PH123 data set appeared similar in nature to the PLC-δ1 set.

The analytical methods ASPT and SFDA were validated for detection of single-molecule data sets and should prove useful for studies in cell biology as they remove bias of manual detection and tracking methods. Fast runtimes mean that data sets can be analyzed within minutes so results can be viewed during the course of an experiment. An ability to gather large data sets is critical to single-molecule analysis. Analysis of data sets from live-cell imaging allows tests of specific molecular mechanisms in cell biology such as understanding the diffusive behavior of membrane-bound proteins and of receptor-ligand interactions. To extend this study and increase our understanding of the enzymology of PLC-δ1 it would be very advantageous to obtain simultaneous data of phosphatitidyl-inositol 4,5-bisphosphate headgroups interacting with the individual PLC-δ1.

APPENDIX

Single fluorophore detection algorithm

We assume that video data consist of a sequence of pixilated images obtained using continuous or time-lapse imaging. The intensity at a given x,y pixel coordinate varies as a function of time, t, $f(x,y,t)$ and at the high magnifications used, individual fluorophores give a Gaussian-shaped intensity profile in the x-y plane that extends over a number of pixels (Fig. 1 *A*). Fluorescence intensity recorded on these pixels will change in a correlated way when a fluorescent object appears or disappears on the image. Camera noise has a high spatial frequency and adjacent pixels are affected in an uncorrelated way. This means that low-pass or smoothing filters (29,30) can be applied to reduce noise. Low-pass filtering can be implemented either using Fourier methods, or by local averaging. We employed an averaging method that gives a resulting pixel intensity $g(x,y)$ corresponding to the local mean of pixels in a surrounding area, S. The dimensions of S approximate the size of a single fluorophore image, which has a diffraction-limited PSF of known size. Assuming that the image pixels are square, S should have equal dimensions in the x-y plane and for computational ease, should be set to the nearest odd number (3, 5, 7...) of pixels that satisfy the PSF size requirement. For example, our imaging system gives a diffraction-limited PSF with FWHM ~300 nm at the object plane, this corresponds to 3 linear pixels at the imaging plane. So, an area, S, of 5 × 5 pixels is used to capture >90% of the intensity emanating from a single fluorophore (i.e. about twice the FWHM). The averaging function can be expressed as Eq. 1.

$$g(x,y) = \frac{1}{S^2} \sum_{y-(S-1)/2}^{y+(S-1)/2} \sum_{x+(S-1)/2}^{x+(S-1)/2} f(x,y). \qquad (1)$$

The intensity distribution produced by an ideal single fluorophore is the same as the PSF of the imaging system and this can be directly measured using control specimens. Using a template or kernel that matches the known PSF the pattern can be identified in the images. We experimented with different arbitrary kernel functions, $w(i,j)$, in an effort to preserve intensity corresponding to a single fluorophore but reduce camera noise. The kernel shown in Fig. 1 *B* gave the best balance between filtering characteristics and computational speed. The kernel operation computes the normalized product of $f(x,y)$ and $w(i,j)$, where, N, is the normalization factor and $g(x,y)$ is the output value. The operation is repeated over all pixels in the image (see Eq. 2):

$$g(x,y) = \frac{1}{N} \sum_{y-(S-1)/2}^{y+(S-1)/2} \sum_{x-(S-1)/2}^{x+(S-1)/2} [f(x,y) \times w(i,j)]. \qquad (2)$$

In real-life imaging applications, noise of low spatial and temporal frequency is also a problem. This arises from uneven spatial illumination of the specimen, temporal variation in the background signal (e.g., photobleaching of cell autofluorescence), or spatiotemporal fluctuations produced by large fluorescent objects drifting across the field of view (see, e.g., Fig. 6 *A*). To

correct for these less well-characterized sources of noise, average fluorescence in an area, S', immediately surrounding the area, S, (centered at x,y) was subtracted. The kernel shown in Fig. 1 *C* performs the combined operation of averaging within the area S together with local background subtraction using the immediate surrounding region S'. The result of this operation should give unity gain, band-pass spatial filtering. Further temporal normalization can give dynamic black-level restoration. Modern personal computers perform floating-point arithmetic with sufficient speed to make this type of filter suitable for large video data records. For example, our data records are of the order 2 Gb; consisting of ~1000 frames at 1000 × 1000 pixels, digitized at 12-bit resolution. The filtering operations require a few minutes to complete.

The next phase of the SFDA is to specifically identify single fluorophore signals from other signals, including those arising from clusters of multiple fluorophores. We know that a single fluorophore will emit a steady number of photons per second under constant illumination before it suddenly and irreversibly photobleaches. So, we expect the signal to exhibit a stepwise drop in intensity to background level that is correlated amongst pixels in the area S, (Fig.1, *E* and *F*, (*upper*) show typical experimental observations). Provided the fluorophore does not move in the x-y plane during data collection, then a temporal ''edge detection'' algorithm can be used to automate identification of such events in a sequence of video data. The best approach is to compute the derivative of the intensity data for each pixel in time. However, because the derivative is very sensitive to noise (29) it should be computed after the filtering operation. Different weightings can be used (e.g., Prewitt or Sobel filters) and window size (measured as the number of frames, L) can be scaled to suit the background noise characteristics. The optimized kernel, $v(t)$, used for our data records is shown in Fig. 1 *D*. This was used to find the local derivative of intensity data at pixel, $g(x,y,t)$, from the immediately preceding and subsequent pixel data. The computational operation is given in Eq. 3.

$$d(x,y,t') = \sum_{t}^{L}[g(x,y,t) \times v(t)]. \quad (3)$$

The kernel $v(t)$ of length, L, is moved along the time axis to give $d(x,y,t')$ for pixels in the resulting three-dimensional image. Positive d-values represent sudden drops and negative values sudden rises in pixel intensity (Fig. 1, *E* and *F* (*lower*)). The most positive value of $d(x,y,t')$ calculated in area around every pixel(x,y) is stored in so-called ''drop mask'', $d_d(x,y)$, which has the sizes of original image f (e.g., Fig. 5 *B*). The most negative value of $d(x,y,t')$ is stored in the corresponding position of so-called ''rise mask'', $d_r(x,y)$. These values are stored together with the time at which these transitions occur. The d_d and d_r arrays can be visualized by representing values on a pseudocolor intensity scale (please note that d_r values should be inversed to show absolute values). This reveals localized spots with the same shape and size as the single fluorophore intensities in the original intensity data records, $f(x,y)$ (e.g., Fig. 5 *B*). However, the data represented in this way have a much higher signal/noise ratio and can be readily thresholded to yield a mask representing the (x,y,t) coordinates at which individual fluorophores appear and disappear (Fig. 5 *C*). Fluorophores that appear during a record can therefore be separated from those that were present right from the very start of the record (see Fig. 1, *E* and *F*). Furthermore, by using the unthresholded ''drop'' and ''rise'' masks, $d(x,y)$, the location of the central pixel can be computed either by finding the local maximum value or by more sophisticated centroid fitting to give subpixel resolution localization (22,31) (Fig. 5 *E*).

Knowing the x,y centroid of each individual fluorophore the original time-series intensity data averaged over its occupied area, S, (i.e., $g(x,y)$) is then extracted from the original video record. Intensity data can be corrected for local background variation by subtracting intensity data from the surrounding region S' (as described earlier). To perform further statistical testing of the data it is useful to calculate the variance (v) of the signal during intervals of high (v_{high}) and low (v_{low}) fluorescence (Eqs. 4 and 5). This analysis allows one to test if the background intensity (g_{low}) and putative fluorophore signal (g_{high}) are statistically significantly different.

$$v_{high}(x,y) = \frac{1}{t_{high}-1}\sum^{t_{high}}[g(x,y,t) - g_{high}(x,y)]^2 \quad (4)$$

$$v_{low}(x,y) = \frac{1}{t_{low}-1}\sum^{t_{low}}[g(x,y,t) - g_{low}(x,y)]^2. \quad (5)$$

The calculated $g_{high}(x,y)$, $g_{low}(x,y)$, $v_{high}(x,y)$, and $v_{low}(x,y)$ values give a statistical measure of the SNR (16), I, and this can be set as a thresholding parameter to discriminate between real and false objects (Fig. 5 *D* and Eq. 6):

$$I(x,y) = \frac{g_{high}(x,y) - g_{low}(x,y)}{\sqrt{v_{high}(x,y) + v_{low}(x,y)}}. \quad (6)$$

Because $I(x,y)$ measures the change in signal level relative to the combined background and signal variances its value gives a more meaningful estimate of signal/noise than if background noise level was considered alone. We found a common problem encountered in live-cell imaging experiments is that discrete background fluorescent material and cell autofluorescence can produce short-lived ''false'' events that contribute additional noise. To deal with this problem, events lasting less than a minimum duration, t_{min}, were excluded. A consequence of this is that a proportion of ''real'' (but short-lived) events will also be excluded, along with the false events. The number of missing real events that are erroneously excluded because they last $<t_{min}$ can be estimated by extrapolating the lifetime distribution plots obtained from analysis of the long-lived events (data not shown), which we detect with more certainty, or alternatively by analysis of simulated or modeled data sets (see Results section above) in which we know a priori what is noise and what is signal. Clearly, relying solely on simulated data sets can lead to circularity in the arguments, so we have used both approaches.

The final part of the SFDA algorithm is to output information about all of the detected objects (whose I value is above a certain threshold, e.g., 95% certainty) including all the raw data; fluorescence intensity, timing, and x,y coordinates. This is stored in an output format suitable for further analysis in statistical packages or Excel spreadsheets.

Automatic single particle tracking

The first phase of the ASPT works by pattern-matching regions of the image to the known PSF of a single fluorophore. The software compares the area around every pixel with a kernel composed of a two-dimensional representation of the idealized single fluorophore PSF. The idealized kernel, $w(i,j)$, is constructed from real data, obtained from the averaged signal produced by a single fluorophore or, is generated from a Gaussian function (Eq. 7) that approximates the PSF using δ determined by averaging the images of real single fluorophores (Fig. 2 *A*, *inset*).

$$w(i,j) = \frac{1}{2\pi\delta^2}e^{\left(-\frac{i^2+j^2}{2\delta^2}\right)}. \quad (7)$$

The local mean-squared deviation to this test kernel (scaled to its best-fit amplitude) was calculated for every pixel (Eq. 8). We found that the kernel size (e.g., test area) should be ~3× the PSF, FWHM size; in our case this was 11 × 11 pixels (~1 × 1 μm). Each pixel in the image is therefore tested for its goodness-to-fit to an idealized fluorophore centroid. This gives a new image $q(x,y)$ in which every pixel intensity value is now set to the inverse mean-squared deviation to an idealized single fluorophore image (see Fig. 2 *B*)

$$q(x,y) = g(x,y)/\sqrt{\left(\sum_{y-(S-1)/2}^{y+(S-1)/2}\sum_{x-(S-1)/2}^{x+(S-1)/2}[f(x,y) - w(i,j)]^2\right)/N}. \quad (8)$$

By thresholding the $q(x,y)$ data (Q_{min}), a list of identified objects can then be stored. The procedure is then repeated for all images in the video sequence.

The second phase of the ASPT routine links object coordinates in adjacent video frames using a nearest-neighbor algorithm. Essentially, each identified object is linked to an object on the adjacent (i.e., subsequent or preceding) frame on the basis of its being the nearest new x,y coordinate. A maximum displacement of radius, r_{max}, limits the range of possible movement between two observation points. Two different methods can be used to find the nearest neighbor: 1), Pixels are searched within a radius, r_{max}, around the current x,y coordinate on the current image frame (Fig. 2 *B*, *inset*). The closest object found on the following frame is linked to the current object. If no object is found, then the object track is terminated. 2), The distances between all objects on adjacent frames is used to identify the closest objects between frames; if the distance exceeds r_{max}, then the track is terminated.

It is important to adjust imaging conditions so that the average distance between nearest fluorescent molecules within a single frame is significantly larger than r_{max}. This is achieved by increasing the imaging rate or by choosing specimens that have fewer fluorescent objects per unit area. The second nearest-neighbor algorithm works much faster than the first one if the density of objects is low and r_{max} is big. For example: if we have 10–20 objects per 100×100 pixels area and predicted r is equal to 10–12 pixels. However, if we have 100–200 objects per 100×100 pixels area and r_{max} is equal to 1–2 pixels then the first method is significantly faster.

Occasionally, objects ''drop out'' from one or more adjacent frames and then reappear, presumably due to fluorophore blinking and this gives rise to ''orphan'' tracks. These tracks can be manually restored in later analysis but were usually discarded on the basis that a valid track must contain more than some minimal number of observation points (n_{min}). We found that setting $n_{min} = 10$ data points, worked well to reduce the number of ''false'' tracks caused by noise. During the first pass of the ASPT algorithm fluorophores are identified on the basis of their size, shape, and intensity (Eq. 8). During the second pass, a nearest-neighbor tracking procedure generates the x,y,t coordinates of each fluorophore track. The original intensity data, $f(x,y,t)$, are then used to refine estimates of fluorophore positions with subpixel resolution. This is done in the same way as for the SFDA routine (described above) (31). Finally, to discriminate between single fluorophores and small multifluorophore clusters (with the same limiting PSF) the original intensity data are inspected to ensure that each object exhibits single-step appearance and disappearance (photobleaching) and has an average intensity similar to that of known single fluorophores measured in our in vitro control specimens.

We thank Dr. Andrea Knowles, MRC National Institute for Medical Research, UK for help with cell culture, Professor Peter Downes, University of Dundee, UK, for providing the eGFP-PLC-δ1 construct, and Dr. Michelle Peckham, University of Leeds, UK, for the eGFP-PH123 constructs and also for helping to initiate this work. The computer software described in this article is available for academic use upon request; please contact: gmashan@nimr.mrc.ac.uk or visit http://www.nimr.mrc.ac.uk/gmimpro.

The authors thank the Medical Research Council, UK, for financial support and confirm that they have no competing financial interests.

REFERENCES

1. Funatsu, T., Y. Harada, M. Tokunaga, K. Saito, and T. Yanagida. 1995. Imaging of single fluorescent molecules and individual ATP turnovers by single myosin molecules in aqueous solution. *Nature.* 374: 555–559.
2. Tsien, R. Y. 1998. The green fluorescent protein. *Annu. Rev. Biochem.* 67:509–544.
3. Harms, G. S., L. Cognet, P. H. M. Lommerse, G. A. Blab, and T. Schmidt. 2001. Autofluorescent proteins in single-molecule research: applications to live cell imaging microscopy. *Biophys. J.* 80: 2396–2408.
4. Axelrod, D. 1992. Total Internal Reflection Fluorescence. Plenum Press, New York.
5. Sako, Y., S. Minoghchi, and T. Yanagida. 2000. Single-molecule imaging of EGFR signalling on the surface of living cells. *Nat. Cell Biol.* 2:168–172.
6. Iino, R., I. Koyama, and A. Kusumi. 2001. Single molecule imaging of green fluorescent proteins in living cells: E-cadherin forms oligomers on the free cell surface. *Biophys. J.* 80:2667–2677.
7. Mashanov, G. I., D. Tacon, M. Peckham, and J. E. Molloy. 2004. The spatial and temporal dynamics of pleckstrin homology domain binding at the plasma membrane measured by imaging single molecules in live mouse myoblasts. *J. Biol. Chem.* 279:15274–15280.
8. Sako, Y., and T. Yanagida. 2003. Single-molecule visualization in cell biology. *Nat. Cell Biol.* Suppl:SS1–SS5.
9. Lomasney, J. W., H. F. Cheng, L. P. Wang, Y. S. Kuan, S. M. Liu, S. W. Fesik, and K. King. 1996. Phosphatidylinositol 4,5-bisphosphate binding to the pleckstrin homology domain of phospholipase C-delta 1 enhances enzyme activity. *J. Biol. Chem.* 271:25316–25326.
10. Balla, T., T. Bondeva, and P. Varnai. 2000. How accurately can we image inositol lipids in living cells? *Trends Pharmacol. Sci.* 21:238–241.
11. Sheets, E. D., G. M. Lee, R. Simson, and K. Jacobson. 1997. Transient confinement of a glycosylphosphatidylinositol-anchored protein in the plasma membrane. *Biochemistry.* 36:12449–12458.
12. Veigel, C., M. L. Bartoo, D. C. S. White, J. C. Sparrow, and J. E. Molloy. 1998. The stiffness of rabbit skeletal actomyosin cross-bridges determined with an optical tweezers transducer. *Biophys. J.* 75:1424–1438.
13. Mashanov, G. I., D. Tacon, A. E. Knight, M. Peckham, and J. E. Molloy. 2003. Visualizing single molecules inside living cells using total internal reflection fluorescence microscopy. *Methods.* 29:142–152.
14. Schutz, G. J., H. Schindler, and T. Schmidt. 1997. Single-molecule microscopy on model membranes reveals anomalous diffusion. *Biophys. J.* 73:1073–1080.
15. Press, W. H., S. A. Teukolsky, W. T. Vetterling, and B. P. Flannery. 1992. Numerical Recipes in C. The Art of Scientific Computing. Cambridge University Press, Cambridge, United Kingdom.
16. Koyama-Honda, I., K. Ritchie, T. Fujiwara, R. Iino, H. Murakoshi, R. S. Kasai, and A. Kusumi. 2005. Fluorescence imaging for monitoring the colocalization of two single molecules in living cells. *Biophys. J.* 88:2126–2136.
17. Kues, T., R. Peters, and U. Kubitscheck. 2001. Visualization and tracking of single protein molecules in the cell nucleus. *Biophys. J.* 80:2954–2967.
18. Anderson, C. M., G. N. Georgiou, I. E. G. Morrison, G. V. W. Stevenson, and R. J. Cherry. 1992. Tracking of cell-surface receptors by fluorescence digital imaging microscopy using a charge-coupled device camera: low-density-lipoprotein and influenza-virus receptor mobility at 4-degrees-C. *J. Cell Sci.* 101:415–425.
19. Cherry, R. J., P. R. Smith, I. E. G. Morrison, and N. Fernandez. 1998. Mobility of cell surface receptors: a re-evaluation. *FEBS Lett.* 430:88–91.
20. Ghosh, R. N., and W. W. Webb. 1994. Automated detection and tracking of individual and clustered cell surface low density lipoprotein receptor molecules. *Biophysj. J.* 66:1301–1318.
21. Thomann, D., D. R. Rines, P. K. Sorger, and G. Danuser. 2002. Automatic fluorescent tag detection in 3D with super-resolution: application to the analysis of chromosome movement. *J. Microsc.* 208: 49–64.
22. Gelles, J., B. J. Schnapp, and M. P. Sheetz. 1988. Tracking kinesin-driven movements with nanometre-scale precision. *Nature.* 331:450–453.
23. Schutz, G. J., V. P. Pastushenko, H. J. Gruber, H. Knaus, and H. Schindler. 2000. 3D imaging of individual ion channels in live cells at 40 nm resolution. *Single Mol.* 1:25–31.
24. Peters, R., and R. J. Cherry. 1982. Lateral and rotational diffusion of bacteriorhodopsin in lipid bilayers: experimental test of the Saffman-Delbruck equations. *Proc. Natl. Acad. Sci. USA.* 79:4317–4321.
25. Philip, F., Y. J. Guo, and S. Scarlata. 2002. Multiple roles of pleckstrin homology domains in phospholipase C beta function. *FEBS Lett.* 531: 28–32.

26. Martin, T. F. J. 2001. PI(4,5)P-2 regulation of surface membrane traffic. *Curr. Opin. Cell Biol.* 13:493–499.

27. Viswanathan, G. M., S. V. Buldyrev, S. Havlin, M. G. E. da Luz, E. P. Raposo, and H. E. Stanley. 1999. Optimizing the success of random searches. *Nature*. 401:911–914.

28. Simson, R., E. D. Sheets, and K. Jacobson. 1995. Detection of temporary lateral confinement of membrane-proteins using single-particle tracking analysis. *Biophys. J.* 69:989–993.

29. Gonzales, R. C., and R. E. Wood. 2002. Digital Image Processing. Prentice Hall, Upper Saddle River, New Jersey.

30. Seul, M., L. O'Gorman, and M. J. Sammon. 2000. Practical Algorithms for Image Analysis. Cambridge University Press, Cambridge, United Kingdom.

31. Cheezum, M. K., W. F. Walker, and W. H. Guilford. 2001. Quantitative comparison of algorithms for tracking single fluorescent particles. *Biophys. J.* 81:2378–2388.